Data-driven modeling and control of perovskite deposition for solar cells ⋆

Eva Masero *, **Juan D. Zambrano-Torres** *, **Joachim Vollbrecht** **, **J. M. Maestre** ***

* *Dept. of Electronics, Information and Bioengineering, Politecnico di Milano, Milan, Italy (e-mails: {eva.masero, 10815797}@polimi.it).*
** *Dept. of Photovoltaics, Institute for Solar Energy Research Hamelin, Emmerthal, 31860, Germany (e-mail: vollbrecht@isfh.de).*
*** *Dept. of Systems and Automation Engineering, University of Seville, Seville, 41092, Spain (e-mail: pepemaestre@us.es).*

Abstract: Precise control of thin-film deposition is essential in perovskite solar cell manufacturing. This work presents data-driven strategies based on Model Predictive Control (MPC) and Predictive Reference Governor (PRG) to regulate temperature and deposition rate during the perovskite thin-film deposition process while explicitly handling operational constraints. First, a grey-box model of the process is identified from experimental data and integrated into an MPC controller. In parallel, a PRG strategy enhanced with a Kalman filter is proposed to retain the built-in Proportional–Integral–Derivative (PID) controller while enforcing operational constraints and ensuring accurate setpoint tracking. Simulation results show that the proposed MPC and PRG approaches improve tracking performance compared with conventional PID control, thanks to their predictive capability. Finally, a hardware-in-the-loop implementation of the PRG in a Raspberry Pi confirms suitability for embedded deployment.

Keywords: Grey-Box Modeling; Model Predictive Control; Reference Governor; Perovskite Deposition; Chemical Process Control.

1. INTRODUCTION

The fabrication of high-efficiency perovskite solar cells requires precise control of thin-film deposition (Zhang et al., 2024). Indeed, the deposition rate must be tightly controlled for the uniformity, composition accuracy, and crystallinity of the solar cells. However, conventional industrial controllers often struggle to maintain performance under nonlinearities, delays, and strict safety limits.

Pilot-scale perovskite manufacturing systems typically comprise: (i) a thermal evaporation system with a high-vacuum chamber and independently heated sources, (ii) a Quartz Crystal Microbalance (QCM) sensor for real-time deposition rate monitoring, and (iii) an electrical power supply to heat the crucible containing the source materials. This manufacturing process enables solvent-free deposition, controlled film uniformity, and multi-layer fabrication via both co-evaporation and sequential processes. Such capabilities make it particularly relevant for high-performance optoelectronics and photovoltaics, where reproducible stoichiometry and thickness control over large areas are critical (Kosasih et al., 2022).

From a control viewpoint, thermal evaporation presents a challenging combination of multi-timescale dynamics due to the interplay between slow heater/substrate temperature evolution and rapid changes in vapor flux (Flint et al., 2020). The process is further complicated by nonlinear, input-dependent behavior related to precursor volatility thresholds (Lim and Kim, 2020), inter-source coupling in co-evaporation setups, measurement noise, occasional QCM signal dropouts, and strict operational constraints on power, temperature, and rate. These factors limit the effectiveness of conventional Proportional–Integral–Derivative (PID) controllers, which are well-suited to local linear dynamics but cannot proactively enforce constraints or optimize transients in the presence of coupling and delays.

To overcome the limitations of traditional industrial controllers, this work aims to enhance the precision of perovskite deposition through advanced control strategies, such as Model Predictive Control (MPC) and Predictive Reference Governor (PRG), which, to the best our knowledge, still remain unexplored for this process. These controllers rely on a predictive model identified from experimental data obtained in a pilot-scale perovskite manufacturing process. The main contributions are: (i) identification of a macroscopic, grey-box model of the process, (ii) design of MPC and PRG strategies to improve performance over the built-in PID controller, and (iii) development of a hardware-in-the-loop approach in an embedded platform to assess practical implementability.

⋆ Financial support for the MICS project (CUP: D43C22003120001) funded by the Next-Generation EU program (Italian PNRR-M4 C2, Invest 1.3-D.D.1551.11-10-2022, PE00000004); for the NextGenPV grant funded by the State of Lower Saxony; and for C3PO-R3 project (grant PID2023-152876OB-I00) funded by the MCIN/AEI/10.13039/501100011033 and ERDF/EU, is gratefully acknowledged. (*Corresponding author: Eva Masero*).

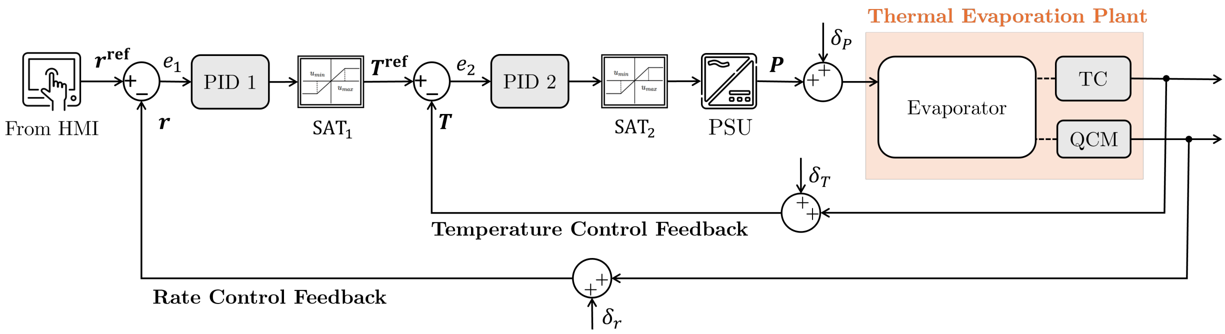

Fig. 1. Schematic of the thermal evaporation process with cascade PID control for temperature and deposition rate, including an HMI for recipe management and data recording. Actuators and sensors noises $\delta_P, \delta_T, \delta_r$ are also shown.

2. SYSTEM DESCRIPTION

The thermal evaporation process consists of a controlled deposition of chemical compounds on the substrate. Moreover, co-evaporation and sequential evaporation are two key techniques for perovskite-based solar cell fabrication that influence film quality, composition, and device performance. In this work, we focus on the thermal evaporation process for perovskite formation that involves three sequential steps: the evaporation of a hole transport material (SpiroTTB), the co-evaporation of inorganic salts (PbI_2 and CsBr), and the evaporation of an organic compound (FAI). The process uses the MiniSpectros system (Kurt J. Lesker Company, 2025), equipped with a cascade control scheme with two PID controllers to regulate temperature and deposition rate for each material in the crucible.

As illustrated in Fig. 1, the thermal evaporation plant receives a power input P, while the temperature T (°C) and deposition rate r (Å/s) of the involved chemical compounds are, respectively, measured using a ThermoCouple (TC) and a QCM. In this cascade PID control scheme, the outer loop compares the measured deposition rate with the rate reference r^{ref} to compute the temperature reference T^{ref} for the inner loop. The inner loop contains a second PID controller that determines a control action expressed as a percentage of the nominal power. This control signal is sent to the Power Supply Unit (PSU), which efficiently transfers power to the evaporator heater by adjusting its temperature. By doing so, the system indirectly regulates the deposition rate through temperature control.

3. MODELING PROCEDURE

A grey-box model of the thermal and deposition dynamics was identified from experimental data obtained in a pilot-scale perovskite manufacturing process at the Institute for Solar Energy Research Hamelin (ISFH). The ISFH datasets comprise 1 s sampled data from two thermal evaporation processes:

- One full perovskite deposition (SpiroTTB, PbI_2+CsBr co-evaporation, and FAI).
- Fourteen PbI_2 evaporations conducted at different deposition rate setpoints: 0.5, 2, 2.25, 3 [Å/s].

The datasets include measurements of power input, vacuum chamber temperature, deposition rate, and instantaneous and accumulated thickness, along with metadata,

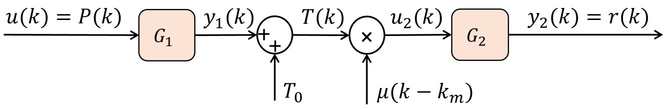

Fig. 2. Block diagram of piecewise grey-box model.

e.g., rate setpoints and PID gains for some compounds. To ensure reliable model estimation, the data were first preprocessed to address noise, outliers, and missing values. This included signal trimming, zero-offset correction, and noise filtering to remove high-frequency disturbances.

The process was modeled following the cascade structure with temperature and deposition rate loops (see Fig. 1). Therefore, the plant was represented by two interconnected subsystems, each discretized at 1 s. The first subsystem, in discrete-time state-space (SS) form:

$$G_1 : \begin{cases} x_1(k+1) = A_1 x_1(k) + B_1 u_1(k) \\ y_1(k) = C_1 x_1(k) + D_1 u_1(k) \end{cases}$$

represents the relationship between the power input $u_1 = P$ and temperature $y_1 = T$, while the second subsystem:

$$G_2 : \begin{cases} x_2(k+1) = A_2 x_2(k) + B_2 u_2(k) \\ y_2(k) = C_2 x_2(k) \end{cases}$$

captures the relationship between the temperature input $u_2 = T$ and deposition rate $y_2 = r$.

By analyzing the temperature responses from the dataset, subsystem G_1 can be effectively modeled as a 1st-order system. Regarding G_2, the deposition rate at the substrate is delayed by a shutter, which blocks material flow until temperature and evaporation rates reach the target thresholds. Once opened, the rate typically exhibits overshoot and damping, suggesting at least a 2nd-order model, and may also show an undershoot (as observed in the organic compound data), indicating non-minimum phase behavior. Consistent with Yangyao (2021), subsystem G_2 was therefore modeled as a 3rd-order system with one non-minimum phase zero. To account for this delay, a step function $\mu(k-k_m) = \{0 \text{ if } k < k_m, 1 \text{ if } k \geq k_m\}$ was applied to the temperature input, activating the rate dynamics only after the temperature exceeds the material's volatility threshold at time k_m (see Fig. 2).

Combining subsystems G_1 and G_2 yielded a 4th-order system, represented in state-space form as:

$$G : \begin{cases} x(k+1) = A_G\, x(k) + B_G\, u(k) + E_G \\ y(k) = C_G\, x(k) + D_G\, u(k) \end{cases} \tag{1}$$

Table 1. Modeling Accuracy.

FIT %	SpiroTTB	PbI_2	CsBr	FAI
Temperature	92.24 %	91.25 %	87.36 %	81.48 %
Rate	97.66 %	78.92 %	85.23 %	81.44 %

where $x = \left[x_1^\top, x_2^\top\right]^\top \in \mathbb{R}^4$ collects the state of the temperature and rate subsystems, $u \in \mathbb{R}$ denotes the power input P, and $y = [y_1, y_2]^\top = [T, r]^\top$ represents the output. The overall system matrices are:

$$A_G = \begin{bmatrix} A_1 & \mathbf{0}_{1\times 3} \\ \mu(k-k_m)B_2C_1 & A_2 \end{bmatrix}, \quad B_G = \begin{bmatrix} B_1 \\ \mu(k-k_m)B_2D_1 \end{bmatrix}$$
$$E_G = \begin{bmatrix} 0 \\ \mu(k-k_m)B_2T_0 \end{bmatrix}, C_G = \begin{bmatrix} C_1 & \mathbf{0}_{1\times 3} \\ 0 & C_2 \end{bmatrix}, D_G = \begin{bmatrix} D_1 \\ 0 \end{bmatrix}$$

where T_0 (°C) is the initial temperature and k_m is identified from the experimental data. See Appendix A.1 for details of the empirically identified model.

3.1 Model identification and Validation

The available dataset was divided into 60 % for model identification, 20 % for model validation, and 20 % for testing the model's generalization capability. However, for those compounds with limited data, the dataset was only split into 70 % for identification and 30 % for validation.

The parameter estimation of model (1) was performed using MATLAB System Identification Toolbox with the Prediction Error Method (PEM), which minimizes the squared residuals between the measured and simulated outputs. Model validation was then conducted by comparing the identified model output with unseen test data. The quantitative performance metric used to evaluate the model accuracy is the FIT index:

$$\text{FIT } (\%) = 100 \cdot \left(1 - \frac{\|y_j - \hat{y}_j\|}{\|y_j - \bar{y}_j\|}\right), \tag{2}$$

where $\hat{y}_j$ is the predicted model output $j \in \{1, 2\}$, y_j the measured data output and $\bar{y}_i$ its average.

Table 1 indicates the cross-validation FIT percentages for the identified models of each compound. For PbI_2, the temperature dynamics consistently achieved FIT values above 90 %, while the deposition rate dynamics reached around 80 % depending on the volatility temperature window considered. Fig. 3 illustrates the response of the identified model for PbI_2 compared to ground truth. Given the greater availability of experimental data for PbI_2 compared to other materials, the proposed control methods were developed using this compound. An interpolation-based gain-scheduling strategy was applied to models identified from six PbI_2 datasets at a rate reference of 0.5 Å/s. Model details are reported in Appendix A.1.

4. ASSESSED CONTROL METHODS

As thin-film deposition control is essential for the fabrication of high-quality solar cells, the control objective is to regulate the deposition rate to achieve the desired composition and thickness of the perovskite layer. In this section, the PbI_2 model is used in two predictive control strategies that optimize performance while accounting for the rate reference, system dynamics, and operational constraints.

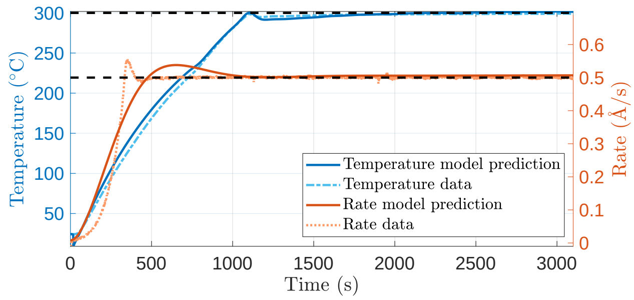

Fig. 3. Model validation for PbI_2: Comparison of the identified model response against experimental data.

4.1 Model Predictive Control

Let $u(n|k)$ denote the predicted power input at step n from time step k, and $\mathbf{u} = [u(k|k), \ldots, u(k+N-1|k)]$ the input sequence over the prediction horizon N. The corresponding predicted state and output trajectories are $\mathbf{x} = [x(k+1|k), \ldots, x(k+N|k)]$ and $\mathbf{y} = [y(k+1|k), \ldots, y(k+N|k)]$. At each k, the goal is to minimize the tracking error and control effort via the cost function:

$$J = \sum_{n=k}^{k+N-1} \left(\|r^{\text{ref}} - y_2(n|k)\|_Q^2 + \|u(n|k)\|_R^2 \right)$$

where r^{ref} denotes the rate reference, y_2 represent the rate, and $Q \succeq 0$ and $R \succ 0$ are tunable weights. In particular, high Q prioritizes reference tracking, while high R limits aggressive control actions to prevent actuator saturation.

The MPC problem is formulated as follows:

$$\mathbf{u}^* = \arg\min_{\mathbf{u}} J(\mathbf{x}, \mathbf{y}, \mathbf{u}) \tag{3a}$$
$$\text{s.t.} \quad x(k|k) = x(k), \tag{3b}$$
$$x(n+1|k) = A_G\, x(n|k) + B_G\, u(n|k) \tag{3c}$$
$$y(n|k) = C_G\, x(n|k) + D_G\, u(n|k), \tag{3d}$$
$$u(n|k) \in \mathcal{U}, \quad \forall n \in [k, k+N-1], \tag{3e}$$

where $x(k)$ is the current state and A_G, B_G, C_G, D_G are the global system matrices. This control model considers only post-threshold dynamics, i.e., once the volatility temperature is reached, and omits the term E_G in (1), which represents an initial temperature offset that is instead absorbed into the state initialization. Constraint (3e) with $\mathcal{U} \triangleq \{u \in \mathbb{R} \mid 0 \le u \le u_{\max}\}$ limits heating power to ensure safety operation. After solving the MPC problem, only the first control action $u(k) = \mathbf{u}^*(k|k)$ is applied to the system. Simulation results are later compared with the built-in PID and the PRG approaches.

4.2 Predictive Reference Governor

The adoption of a reference governor strategy in the MiniSpectros system is motivated by architectural constraints. The built-in cascade PID control cannot be removed due to cost, technical complexity, and safety considerations, making a full control redesign impractical. Instead, the PRG approach can enhance process performance while preserving the existing architecture by adjusting the reference signals supplied to PIDs. Implementing PRG requires a prediction model of the overall closed-loop system, which must be asymptotically stable to assure proper dynamic behavior and convergence.

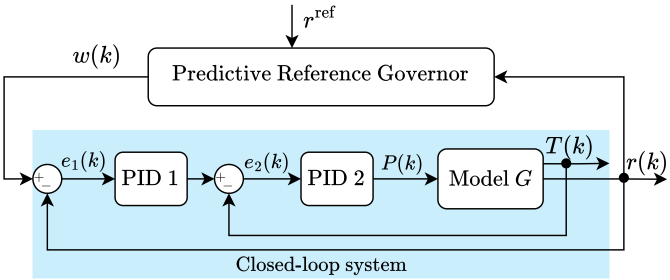

Fig. 4. Scheme of the reference governor approach.

As illustrated in Fig. 4, PRG applies a virtual reference $w(k)$ based on the measured rate $r(k)$ and its reference r^{ref}. The i-th PID output, with gains $K_{\mathrm{P}}, K_{\mathrm{I}}, K_{\mathrm{D}}$, is expressed in terms of its tracking error e_i as:

$$v_i(k) = K_{\mathrm{P}}\Big(e_i(k) + K_{\mathrm{I}}\sum_{t=0}^{k} e_i(t) + K_{\mathrm{D}}\big(e_i(k) - e_i(k-1)\big)\Big)$$

whose state-space representation is:

$$x_{ci}(k+1) = \underbrace{\begin{bmatrix} 0 & K_{\mathrm{P}}K_{\mathrm{I}} \\ 0 & 1 \end{bmatrix}}_{A_{ci}} x_{ci}(k) + \underbrace{\begin{bmatrix} K_{\mathrm{P}}K_{\mathrm{I}} - K_{\mathrm{P}}K_{\mathrm{D}} \\ 1 \end{bmatrix}}_{B_{ci}} e_i(k)$$

$$v_i(k) = \underbrace{[1 \;\; 0]}_{C_{ci}}\, x_{ci}(k) + \underbrace{[K_{\mathrm{P}} + K_{\mathrm{P}}K_{\mathrm{D}}]}_{D_{ci}}\, e_i(k),$$

where $x_{c_i}(k) = [v_i(k), \sum_{t=0}^{k} e_i(t)]^\top \in \mathbb{R}^2$ is the state vector, and $A_{ci}, B_{ci}, C_{ci}, D_{ci}$ are the matrices for $i \in \{1, 2\}$.

Both PID dynamics and the control-oriented model G are captured within a unified closed-loop system:

$$H : \begin{cases} x_H(k+1) = A_H\, x_H(k) + B_H\, w(k) \\ y_H(k) = C_H\, x_H(k) + D_H\, w(k) \end{cases} \tag{4}$$

where the aggregated state is $x_H = \left[x_{c1}^\top, x_{c2}^\top, x^\top\right]^\top \in \mathbb{R}^{8\times 1}$, the input is the virtual reference $w \in \mathbb{R}$, the output is $y_H = [y_{H1}, y_{H2}] = [T, r] \in \mathbb{R}^2$, and the matrices are $A_H \in \mathbb{R}^{8\times 8}, B_H \in \mathbb{R}^{8\times 1}, C_H \in \mathbb{R}^{2\times 8}, D_H \in \mathbb{R}^{2\times 1}$. See Appendix A.2 for specific parameters of the model.

Since PRG relies on access to the closed-loop state, which is not directly measured, a state observer is used to estimate $x_H(k)$ from input $w(k)$ and measured output $y_H(k)$. In particular, a Kalman Filter (KF) observer is designed, assuming that (4) is affected by zero-mean white Gaussian process and measurement noises δ_x and δ_y, respectively, with covariance matrices: $\Phi_x = \sigma^2 I_{8\times 8}$, and $\Phi_y = \begin{bmatrix} 0 & 0 \\ 0 & \sigma^2 \end{bmatrix}$. After verifying that pair (A_H, B_Φ), with $\Phi_y = B_\Phi B_\Phi^\top$, is reachable and the pair (A_H, C_H) is observable, the following state observer is proposed:

$$\begin{aligned} \hat{x}_H(k+1) = & A_H\, \hat{x}_H(k) + B_H\, w(k) \\ & - L\Big(y_H(k) - C_H\, \hat{x}_H(k) - D_H\, w(k)\Big) \end{aligned} \tag{5}$$

where $L \in \mathbb{R}^{8\times 2}$ is the steady-state KF gain obtained from the Riccati equation using the given covariance matrices. The empirical value of L is reported in Appendix A.2.

Building on the work of Klaučo and Kvasnica (2019), in which the virtual reference sequence is optimized over a prediction horizon and applied using a receding-horizon strategy, the PRG problem consists of minimizing J_H:

$$\begin{aligned} J_H = \sum_{n=k}^{k+N-1} \Big(& \|r^{\mathrm{ref}} - y_{H2}(n|k)\|^2_{Q_{\mathrm{ry}}} + \|r^{\mathrm{ref}} - w(n|k)\|^2_{Q_{\mathrm{rw}}} \\ & + \|w(n|k) - y_{H2}(n|k)\|^2_{Q_{\mathrm{wy}}} \\ & + \|w(n|k) - w(n+1|k)\|^2_{Q_{\Delta\mathrm{w}}} \Big) \end{aligned}$$

where $Q_{\mathrm{ry}} \succ 0$ weights the error between the rate reference r^{ref} and the measured rate y_{H2}, $Q_{\mathrm{rw}} \succ 0$ enforces convergence of the virtual reference to the actual one, $Q_{\mathrm{wy}} \succ 0$ penalizes deviations of the closed-loop output from the virtual reference, and $Q_{\Delta\mathrm{w}} \succ 0$ limits reference variations over the prediction horizon.

Let $\mathbf{w} = [w(k|k), \ldots, w(k+N-1|k)]$ and $\mathbf{w}^+ = [w(k+1|k), \ldots, w(k+N|k)]$ denote the virtual reference sequences over N. The PRG problem is formulated as:

$$\mathbf{w}^* = \arg\min_{\mathbf{w}} \quad J_H(\mathbf{y}_H, \mathbf{w}, \mathbf{w}^+) \tag{6a}$$

$$\text{s.t.} \quad x_H(k|k) = \hat{x}_H(k), \tag{6b}$$

$$x_H(n+1|k) = A_H\, x_H(n|k) + B_H\, w(n|k), \tag{6c}$$

$$y_H(n|k) = C_H\, x_H(n|k) + D_H\, w(n|k), \tag{6d}$$

$$w(n|k) \in \mathcal{W}, \quad \forall n \in [k, k+N-1], \tag{6e}$$

where $\hat{x}_H(k)$ is the estimated state at time k, and $\mathcal{W} \triangleq \{w \in \mathbb{R} \mid 0 \le w \le w_{\max}\}$ bounds the virtual reference w to ensure safe operation. The control-oriented model H includes only post-threshold dynamics and the temperature offset related to E_G is incorporated into the initialization of x_H. After solving the PRG problem, the first reference $w(k) = \mathbf{w}^*(k|k)$ is applied to the system (see Fig. 4).

4.3 Simulation results

This section presents simulation results for the built-in PID, MPC, and PRG over a 2000 s simulation with sampling time of 1 s. The rate reference is set to $r^{\mathrm{ref}} = 0.5$ Å/s consistent with the PbI_2 model identification and typical operation. Noise covariance was selected from sensor specifications and data variance, with $\sigma = 13.78 \times 10^{-6}$. For predictive control approaches, a horizon $N = 120$ was chosen to balance performance and computational cost, ensuring real-time implementation of the PRG (see Section 4.4). Experimental data under the cascade PID show that the PbI_2 temperature reaches its volatility threshold (232 °C) at $k_m = 756$ s. The input power is limited to $u_{\max} = 60\,\%$, while the virtual reference is constrained by $w_{\max} = 0.65$ Å/s. For the PID controllers, control gains are extracted from historical data: PID_1 with $K_{\mathrm{P}} = 630$, $K_{\mathrm{I}} = 1/200$, $K_{\mathrm{D}} = 0$, and PID_2 with $K_{\mathrm{P}} = 1.91$, $K_{\mathrm{I}} = 1/393$, $K_{\mathrm{D}} = 1/47$. For MPC, the cost weights are heuristically tuned to balance tracking and control effort, with $Q = 100$ and $R = 1 \times 10^{-7}$. For PRG, the weights are selected to meet performance objectives: $Q_{\mathrm{ry}} = 1300$, $Q_{\mathrm{rw}} = 25$, $Q_{\mathrm{wy}} = 10$, and $Q_{\Delta\mathrm{w}} = 15$.

Performance metrics, including Integral Square Error (ISE), Integral Square Control Output (ISCO) and incre-

Table 2. Comparison of performance metrics.

Metric	PID	MPC	PRG
ISE	54.18	32.97	26.24
ISCO	43×10^5	49.5×10^5	37×10^5
$\mathrm{ISCO}_{\Delta u}$	11.2×10^4	56.37	26×10^2

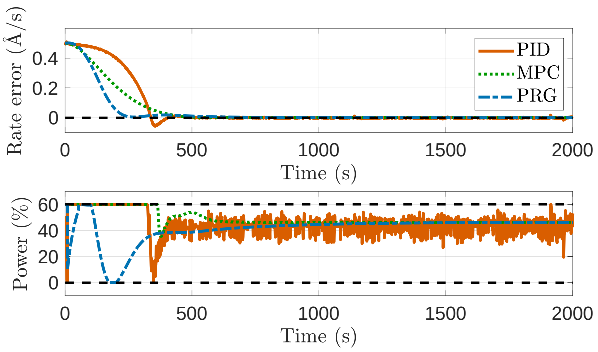

Fig. 5. Tracking error of rate (Å/s) and power signals (%).

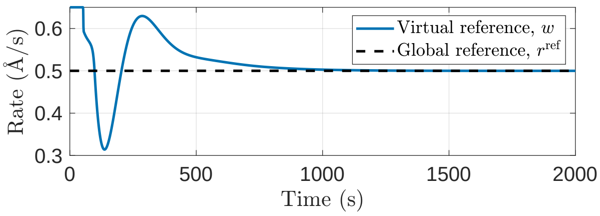

Fig. 6. Optimized virtual reference of PRG over time.

mental ISCO, are calculated as:

$$\text{ISE} = \sum_{k=1}^{M} e_1(k)^2,\ \text{ISCO} = \sum_{k=1}^{M} u(k)^2,\ \text{ISCO}_{\Delta u} = \sum_{k=1}^{M} \big(\Delta u(k)\big)^2$$

where $e_1(k) = r^{\text{ref}} - r(k)$ is the rate error [Å/s], $u(k)$ is the power input P [%], and $\Delta u(k) = u(k) - u(k-1)$. Results in Table 2 show that, relative to PID, MPC reduces ISE by 39.1 % at the cost of a 15.1 % increase in ISCO, while PRG provides a 51.6 % ISE reduction and a 13.86 % ISCO decrease. In terms of actuation smoothness, as quantified by the $\text{ISCO}_{\Delta u}$, MPC exhibits the smoothest actuation with a 99.95 % reduction compared to the PID, whereas PRG achieves a more moderate reduction of 76.7 %.

Fig. 5 compares tracking error and power input for PID (from data), MPC, and PRG approaches. The optimized signal in PRG is the virtual reference $w(k)$ (see Fig. 6), which respects constraints and converges to r^{ref}. As shown in Fig. 5, the MPC response exhibits saturation and oscillations, leading to longer settling times, while the PRG achieves a smoother and faster transient response. Overall, both predictive strategies improve control performance and support enhanced perovskite solar cell manufacturing.

4.4 A path to deployment

The proposed PRG strategy was implemented on a Raspberry Pi to demonstrate real-time embedded optimization for practical deployment. System interfaces and communication protocols between the Raspberry Pi 5 and the Simulink host environment were established via Wi-Fi using UDP over TCP/IP framework. As shown in Fig. 7, current rate and temperature measurements were transmitted from Simulink to the Raspberry Pi, where problem (6) was solved online using CasADi's Python API. Multi-core processing capabilities were exploited to meet the 1 s sampling time. The computed virtual reference was then sent back in real time to Simulink, which executed a hardware-in-the-loop simulation of the thermal evaporation process, thereby closing the control loop.

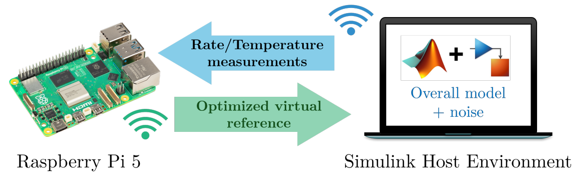

Fig. 7. Hardware-in-the-Loop setup schematic.

This experimental setup confirms that the PRG approach can be effectively deployed on embedded platforms with low latency and limited computational burden, validating its potential for integration in industrial environments.

5. CONCLUSIONS

This work shows that predictive control enhances thermal evaporation for perovskite solar cell deposition. In particular, the proposed MPC and PRG strategies reduce the integral squared error of over 39 % and 51 %, respectively, compared to PID, while also lowering control effort. From a practical perspective, MPC is preferable when computational resources are sufficient to allow real-time optimization and when smooth actuator operation is critical, while PRG enables straightforward integration into existing industrial facilities without replacing the baseline controller, maintaining competitive performance. As a practical proof of concept, the proposed PRG was implemented on a Raspberry Pi within a hardware-in-the-loop setup. These findings confirm that advanced control methods can improve deposition accuracy, thereby ensuring high-quality perovskite layer formation. Future work will focus on pilot-scale validation and extension to multi-evaporator systems with coupled dynamics.

REFERENCES

Flint, T.F., Scotti, L., Basoalto, H.C., and Smith, M.C. (2020). A thermal fluid dynamics framework applied to multi-component substrates experiencing fusion and vaporisation state transitions. *Commun. Phys.*, 3, 196.

Klaučo, M. and Kvasnica, M. (2019). *MPC-Based Reference Governors*. Springer.

Kosasih, F.U., Erdenebileg, E., Mathews, N., Mhaisalkar, S.G., and Bruno, A. (2022). Thermal evaporation and hybrid deposition of perovskite solar cells and mini-modules. *Joule*, 6(12), 2692–2734.

Kurt J. Lesker Company (2025). Mini SPECTROS Thin Film Deposition System Platform. `https://www.lesker.com/process-equipment-division/thin-film-systems/mini-spectros-deposition-platform.cfm`. Accessed: 29-July-2025.

Lim, S.H. and Kim, H.K. (2020). Deposition rate effect on optical and electrical properties of thermally evaporated wo3- x/ag/wo3- x multilayer electrode for transparent and flexible thin film heaters. *Sci. Reports*, 10(1), 8357.

Yangyao, D. (2021). *Microscopic Modeling, Machine Learning-Based Modeling and Optimal Operation of Thermal and Plasma Atomic Layer Deposition*. Ph.D. thesis, University of California(UCLA).

Zhang, J. et al. (2024). Precise control of process parameters for > 23% efficiency perovskite solar cells in ambient air using an automated device acceleration platform. *Energy & Environmental Science*, 17(15), 5490–5499.

Appendix A. MODELING

This appendix includes the detailed state-space model matrices for the PbI_2 material, which has been identified with the experimental data provided by the Institute for Solar Energy Research Hamelin (ISFH).

A.1 Grey-box model

The empirically matrices identified for the open-loop model (1) for PbI_2 are the following:

$$A_G = \begin{bmatrix} 0.9985 & \mathbf{0}_{1\times 3} \\ \mu(k-756)\cdot\begin{bmatrix} -3.72\times 10^{-6} \\ 0 \\ 0 \end{bmatrix} & \begin{bmatrix} 0.9882 & 0.999 & -0.9874 \\ 1 & 0 & 0 \\ 0 & 1 & 0 \end{bmatrix} \end{bmatrix}, B_G = \begin{bmatrix} -1.3529 \\ \mu(k-756)\cdot\begin{bmatrix} -16.84\times 10^{-5} \\ 0 \\ 0 \end{bmatrix} \end{bmatrix},$$

$$E_G = \begin{bmatrix} 0 \\ \mu(k-756)\cdot\begin{bmatrix} 11.7\times 10^{-6} \\ 0 \\ 0 \end{bmatrix} \end{bmatrix}, \quad C_G = \begin{bmatrix} -0.0075 & 0 & 0 & 0 \\ 0 & 64.985\times 10^{-5} & 0 & 0 \end{bmatrix}, \quad D_G = \begin{bmatrix} -0.3449 \\ 0 \end{bmatrix}. \tag{A.1}$$

A.2 Closed-loop model formulation and values

The matrices identified for the closed-loop system (4) are structured as follows:

$$A_H = \begin{bmatrix} A_{c1} & \mathbf{0}_{2\times 2} & -B_{c1}C_2 \\ B_{c2}C_{c1} - \beta B_{c2}D_1D_{c2}D_{c1} & A_{c2} - \beta B_2 D_1 C_{c2} & -B_{c2}D_{c1}C_2 - B_{c2}C_1 + \Sigma \\ \beta B_G D_{c2} C_{c1} & \beta B_G C_{c2} & A_G - \beta B_G D_{c2} D_{c1} C_2 - \beta B_G D_{c2} C_1 \end{bmatrix},$$

$$\Sigma = \beta B_{c2}D_1D_{c2}D_{c1}C_2 + \beta B_{c2}D_1D_{c2}C_1$$

$$B_H = \begin{bmatrix} B_{c1} \\ B_{c2}D_{c1} - \beta B_{c2}D_1D_{c2}D_{c1} \\ \beta B_G D_{c2} D_{c1} \end{bmatrix},$$

$$C_H = \begin{bmatrix} \beta D_G D_{c2} C_{c1} & \beta D_G C_{c2} & C_G - \beta D_G D_{c2} D_{c1} C_2 - \beta D_G D_{c2} C_1 \end{bmatrix}, \quad D_H = \begin{bmatrix} \beta D_G D_{c2} D_{c1} \end{bmatrix},$$

where $\Sigma \in \mathbb{R}^{2\times 4}$, and $\beta = 1/(1 + D_{c2}D_1) \in \mathbb{R}$. Here, $A_{c1} \in \mathbb{R}^{2\times 2}$, $B_{c1} \in \mathbb{R}^{2\times 1}$, $C_{c1} \in \mathbb{R}^{1\times 2}$, $D_{c1} \in \mathbb{R}$ represent the state-space matrices of the external rate controller PID_1, $A_{c2} \in \mathbb{R}^{2\times 2}$, $B_{c2} \in \mathbb{R}^{2\times 1}$, $C_{c2} \in \mathbb{R}^{1\times 2}$, $D_{c2} \in \mathbb{R}$ are those of internal temperature controller PID_2, and $A_G \in \mathbb{R}^{4\times 4}$, $B_G \in \mathbb{R}^{4\times 1}$, $C_G \in \mathbb{R}^{2\times 4}$, $D_G \in \mathbb{R}^{2\times 1}$ are the matrices of plant G. The specific parameters, identified from empirical data, are given below:

$$A_H = \begin{bmatrix} 0 & 3.15 & 0 & 0 & 0 & -2\times 10^{-3} & 0 & 0 \\ 0 & 1 & 0 & 0 & 0 & -6\times 10^{-4} & 0 & 0 \\ -0.1093 & 0 & -3.77\times 10^{-2} & 4.9\times 10^{-3} & -9\times 10^{-4} & 4.48\times 10^{-2} & 0 & 0 \\ 3.056 & 0 & 1.054 & 1 & 2.43\times 10^{-2} & -1.2511 & 0 & 0 \\ -8.0648 & 0 & -4.1345 & 0 & 0.9343 & 3.3018 & 0 & 0 \\ -1\times 10^{-3} & 0 & -5\times 10^{-4} & 0 & 0 & 0.9886 & 0.999 & -0.9874 \\ 0 & 0 & 0 & 0 & 0 & 1 & 0 & 0 \\ 0 & 0 & 0 & 0 & 0 & 0 & 1 & 0 \end{bmatrix},$$

$$B_H = \begin{bmatrix} 3.2 \\ 1 \\ -68.9 \\ 1925.3 \\ -5080.9 \\ -0.6 \\ 0 \\ 0 \end{bmatrix}, \quad C_H = \begin{bmatrix} -2.056 & 0 & -1.054 & 0 & -2.43\times 10^{-2} & 0.8417 & 0 & 0 \\ 0 & 0 & 0 & 0 & 0 & 6\times 10^{-4} & 0 & 0 \end{bmatrix}, \quad D_H = \begin{bmatrix} -1.2953 \\ 0 \end{bmatrix} \times 10^3. \tag{A.2}$$

Furthermore, the Kalman Filter gain used in (5) is $L = \begin{bmatrix} 0.433 & -0.441 \\ 0.137 & -0.140 \\ 0.319 & -0.885 \\ 70.86 & -240.16 \\ -189.4 & 641.75 \\ -3.114 & 16.190 \\ -2.960 & 15.918 \\ -3.103 & 15.614 \end{bmatrix}$.